Monthly Notices
of the
ROYAL ASTRONOMICAL SOCIETY

MNRAS **519,** 3546–3563 (2023)
Advance Access publication 2022 September 12

https://doi.org/10.1093/mnras/stac2565

The EBLM project – IX. Five fully convective M-dwarfs, precisely measured with *CHEOPS* and *TESS* light curves

D. Sebastian [1]★ M. I. Swayne [2] P. F. L. Maxted [2] A. H. M. J. Triaud [1] S. G. Sousa [3] G. Olofsson [4] M. Beck [5] N. Billot [5] S. Hoyer [6] S. Gill,[7] N. Heidari,[6] D. V. Martin [8] C. M. Persson,[9] M. R. Standing [1] Y. Alibert [10] R. Alonso [11,12] G. Anglada [13,14] J. Asquier,[15] T. Bárczy [16] D. Barrado [17] S. C. C. Barros [3,18] M. P. Battley [7] W. Baumjohann [19] T. Beck,[10] W. Benz [10,20] M. Bergomi,[21] I. Boisse [6] X. Bonfils [22] A. Brandeker [4] C. Broeg [10,20] J. Cabrera,[23] S. Charnoz [24] A. Collier Cameron [25] Sz. Csizmadia [23] M. B. Davies [26] M. Deleuil [6] L. Delrez [27,28] O. D. S. Demangeon [3,18] B.-O. Demory [20] G. Dransfield [1] D. Ehrenreich [5] A. Erikson,[23] A. Fortier [10,20] L. Fossati [19] M. Fridlund [9,29] D. Gandolfi [30] M. Gillon [27] M. Güdel,[31] J. Hasiba,[19] G. Hébrard,[32] K. Heng [7,20] K. G. Isaak [33] L. L. Kiss,[34,35] E. Kopp,[23] V. Kunovac [1,47] J. Laskar [36] A. Lecavelier des Etangs [32] M. Lendl [5] C. Lovis [5] D. Magrin [21] J. McCormac,[7] N. J. Miller [2] V. Nascimbeni [21] R. Ottensamer [31] I. Pagano [37] E. Pallé [11] F. A. Pepe,[5] G. Peter [38] G. Piotto [21,39] D. Pollacco,[7] D. Queloz [40,41] R. Ragazzoni [21,39] N. Rando,[15] H. Rauer [23,43,44] I. Ribas [13,14] S. Lalitha [1] A. Santerne [6] N. C. Santos [3,18] G. Scandariato [37] D. Ségransan [5] A. E. Simon [10] A. M. S. Smith [23] M. Steller [19] Gy. M. Szabó,[44,45] N. Thomas,[10] S. Udry [5] V. Van Grootel [28] and N. A. Walton [46]

Affiliations are listed at the end of the paper

Accepted 2022 September 6. Received 2022 August 30; in original form 2022 June 6

ABSTRACT

Eclipsing binaries are important benchmark objects to test and calibrate stellar structure and evolution models. This is especially true for binaries with a fully convective M-dwarf component for which direct measurements of these stars' masses and radii are difficult using other techniques. Within the potential of M-dwarfs to be exoplanet host stars, the accuracy of theoretical predictions of their radius and effective temperature as a function of their mass is an active topic of discussion. Not only the parameters of transiting exoplanets but also the success of future atmospheric characterization relies on accurate theoretical predictions. We present the analysis of five eclipsing binaries with low-mass stellar companions out of a subsample of 23, for which we obtained ultra-high-precision light curves using the *CHEOPS* satellite. The observation of their primary and secondary eclipses are combined with spectroscopic measurements to precisely model the primary parameters and derive the M-dwarfs mass, radius, surface gravity, and effective temperature estimates using the `PYCHEOPS` data analysis software. Combining these results to the same set of parameters derived from *TESS* light curves, we find very good agreement (better than 1 per cent for radius and better than 0.2 per cent for surface gravity). We also analyse the importance of precise orbits from radial velocity measurements and find them to be crucial to derive M-dwarf radii in a regime below 5 per cent accuracy. These results add five valuable data points to the mass–radius diagram of fully convective M-dwarfs.

Key words: techniques: photometric – techniques: spectroscopic – binaries: eclipsing – stars: fundamental parameters – stars: low-mass.

1. INTRODUCTION

Low-mass main-sequence stars of M-type (M-dwarfs) have been in the spotlight of recent exoplanet surveys (Nutzman & Charbonneau 2008; Barclay, Pepper & Quintana 2018; Delrez et al. 2018; Quirrenbach et al. 2019; Donati et al. 2020). This development has two main reasons. First their low masses, and radii, compared to F, G, and K stars make it easier to detect small planets and planetary systems composed of mini Neptunes down to Earth-sized planets by means of radial velocity (RV) and transit methods (e.g. Gillon et al. 2016; Günther et al. 2019; Zechmeister et al. 2019). Thus, more Earth-sized

★ E-mail: D.Sebastian.1@bham.ac.uk

planets have been found in the habitable zone of M-dwarfs than for solar-type stars (e.g. Dressing & Charbonneau 2013). Second, M-dwarfs have low luminosities and, thus offer the first possible window to study transiting rocky planets in their habitable zone and directly analyse their atmospheres with high-precision instruments like the *James Webb Space* telescope (Kaltenegger & Traub 2009; Morley et al. 2017).

Such studies depend crucially on the knowledge of the parameters of M-dwarf planets which in turn are derived from the mass and radius of the host M-dwarf. Up to now our understanding on the mass and radius distribution of low-mass stars which are fully convective ($M_\star < 0.35\,M_\odot$, Chabrier & Baraffe 1997) is rather poorly explored compared to more massive stars. This is mainly due to the relative faintness of these stars.[1] Especially the lack of a large sample of M-dwarfs with directly measured mass and radius make it difficult to calibrate stellar evolution models which are typically used to estimate the properties of planet host stars like for example the Exeter/Lyon models (Baraffe et al. 2015) or the Dartmouth models (Dotter et al. 2008).

Studies of M-stars with available radii and masses have revealed that their stellar radii for a given mass are apparently inflated by a few per cent, compared to estimates from models (e.g. Casagrande, Flynn & Bessell 2008; Torres, Andersen & Giménez 2010; Spada et al. 2013; Kesseli et al. 2018).

Several possible explanations have been discussed, like stellar magnetic activity (Mullan & MacDonald 2001; Chabrier, Gallardo & Baraffe 2007), or a bias due to binarity (Ribas 2006; Morales et al. 2009). Also, metallicity effects seem to play a role (Berger et al. 2006; von Boetticher et al. 2019). Thus, a representative sample of low-mass M-dwarfs with accurately measured mass, radius, and also metallicity is crucial to understand how these different effects enter into this radius inflation problem.

The eclipsing binaries with low mass (EBLM) project (Triaud et al. 2013) is focusing on a large sample with hundreds of eclipsing binaries of F, G, & K-type stars, orbited by late-type M-dwarf companions. These binaries have been detected from the WASP survey (Pollacco et al. 2006). Using a large RV follow-up campaign of these stars, Triaud et al. (2017) derived accurate orbits of many of these systems thus being able to measure fundamental parameters like precise mass and radius of the low-mass M-dwarfs. The binary configuration with a solar-type star allows us to measure accurately the metallicity of the solar-type star. Assuming an equal metallicity of both components, we can constrain the metallicity of the M-dwarf. Thus, EBLM targets are ideal candidates to populate the mass regime of fully convective M-dwarfs with masses below $0.35\,M_\odot$ and to establish an empirical mass–radius–metallicity relationship for these stars. Early results from sub samples indicate that models can be matched quite well, when taking accurate measurements of the metallicity of the M-dwarf into account (Gill et al. 2019; von Boetticher et al. 2019). Every low-mass M-dwarf with accurately measured mass, radius, and metallicity will help to tighten the constraints on the source of the radius inflation problem and in return will allow us in future to constrain precise parameters of planet host stars.

CHEOPS (Benz et al. 2021) is a S-class mission of the European Space Agency, which has been launched on the 2019 December 18. Its primary mission is to perform ultra-high-precision photometry of bright exoplanet host stars. We have started an 'Ancillary Science' programme on a selection of 23 EBLM targets, to obtain precise measurements of primary and secondary eclipses, which allow us to (i) derive the size of both components and (ii) to measure the M-dwarf effective temperature from the surface brightness ratios. Additionally, we use light curves, obtained by the *TESS* survey (Ricker et al. 2015), which covers the Northern and Southern hemispheres with observing periods of about 1 month per pointing (sector). *TESS* cameras have a three times smaller aperture compared to *CHEOPS*, leading to a lower accuracy for eclipse events in *TESS* data. Nevertheless, the long coverage of photometric data allows us to gather multiple eclipses of our targets and thus improve and compare orbital parameters, as well as to optimize our analysis of *CHEOPS* observations.

The three EBLM binaries, analysed in our *CHEOPS* programme EBLM J1741+31, EBLM J1934−42, and EBLM J2046+06 have shown that M-dwarfs with precisely measured radii and metallicities open up the possibility to disentangle the effect of metallicity from different effects on the radius inflation problem for low-mass M-dwarfs (Swayne et al. 2021, hereafter SW21).

In this paper, we present the analysis of five EBLM binaries with fully convective M-dwarfs companions, observed in our *CHEOPS* programme and compare them to the analysis of *TESS* observations.

2. OBSERVATIONS AND METHODS

Primary and secondary eclipses for all our five eclipsing binaries were observed with *CHEOPS* between 2020 November and 2021 January as part of *CHEOPS* Guaranteed Time Observation programme (ID-037). We obtained one primary eclipse and, depending on the depth of the secondary eclipse, one to three secondary eclipse observations in order to obtain sufficient signal-to-noise ratio (SNR) to measure both eclipses. Table 1 gives an overview of the *CHEOPS* observations and data extraction. All data were reduced by the *CHEOPS* data reduction pipeline v13.1 (Hoyer et al. 2020), which performs an aperture photometry of the target star, taking contamination in the field as well as instrumental effects like the rotation of the satellite into account. The pipeline offers light curves for different aperture sizes. For our analysis, we selected the aperture size with minimal median absolute deviation of the point-to-point difference in the light curve. The resulting aperture radii are listed as $R_{\rm ap}$ in Table 1. The observations were interrupted due to the low-Earth-orbit of *CHEOPS* by Earth occultations, as well as crossings of the South Atlantic Anomaly. We derive the time spent on target as the fraction of valid observations compared to the total observation interval.

The *TESS* survey covered all of our targets with 2-min cadence data made available by *TESS* Guest Investigator (GI) programmes. EBLM J0239−20 (TIC64108432) has been observed in sectors 4 and 31 under GI programmes G011278 and G03216. EBLM J0540−17 (TIC46627823) has been observed in sectors 6 and 32 under GI programmes G011278, G03216, and G03251. EBLM J0546−18 (TIC93334206) has been observed in sectors 32 and 33 under GI programme G03216. EBLM J0719+25 (TIC458377744) has recently been observed in sectors 44, 45, and 46 under GI programme G04157, and EBLM J2359+44 (TIC177644756) has been observed in sector 17 under GI programmes G022253 and G022156. Data reduction and light-curve extraction were done by the *TESS* Science Processing Operations Center Pipeline (Jenkins et al. 2016) and were downloaded via the Mikulski Archive for Space Telescopes.[2] For our analysis, we used Pre-search Data Conditioned

[1] E.g. the planet host star TRAPPIST-1, a M7.5 ultra-cool dwarf in 12-pc distance has a visual magnitude of only 18.8 mag.

[2] https://archive.stsci.edu/

Table 1. *CHEOPS* observations and data extraction for our targets. Effic. is the fraction of the observation that resulted in valid (usable) data and R_{ap} the aperture radius used to extract the light curves.

Eclipse Event	Target	Start date (UTC)	Duration (h)	T_{exp} (s)	Effic. (per cent)	File key	R_{ap} (pixels)
Primary	EBLM J0239−20	2020-11-01T15:43	8.80	60	86.2	CH_PR100037_TG012001_V0200	25
Secondary		2020-11-05T20:30	7.99	60	93.2	CH_PR100037_TG011901_V0200	25
Secondary		2020-11-19T17:24	9.02	60	70.4	CH_PR100037_TG011902_V0200	25
Primary	EBLM J0540−17	2020-12-07T08:39	10.04	60	68.4	CH_PR100037_TG012601_V0200	17.5
Secondary		2021-01-21T09:39	10.75	60	54.1	CH_PR100037_TG012502_V0200	17.5
Secondary		2020-12-04T08:13	10.62	60	66.5	CH_PR100037_TG012501_V0200	17.5
Secondary		2021-01-27T09:20	10.49	60	50.0	CH_PR100037_TG012503_V0200	17.5
Primary	EBLM J0546−18	2020-11-30T22:27	8.67	60	67.5	CH_PR100037_TG012801_V0200	25
Secondary		2020-12-31T05:35	8.77	60	66.3	CH_PR100037_TG012701_V0200	25
Secondary		2021-01-09T19:50	8.05	60	64.0	CH_PR100037_TG012702_V0200	25
Primary	EBLM J0719+25	2020-12-10T07:03	8.80	60	52.8	CH_PR100037_TG013001_V0200	22.5
Secondary		2021-02-03T20:54	8.69	60	57.7	CH_PR100037_TG017301_V0200	22.5
Secondary[a]		2020-12-21T12:03	8.50	60	60.2	CH_PR100037_TG012901_V0200	22.5
Secondary	EBLM J2359+44	2020-11-11T08:59	8.89	60	58.3	CH_PR100037_TG016301_V0200	26.5
Primary		2020-11-28T13:07	15.67	60	51.4	CH_PR100037_TG016401_V0200	26.5

Note.
[a]For this observation the secondary eclipse of EBLM J0719+25 has been missed, thus we cannot use this data set for parameter determination of the binary.

Simple Aperture Photometry flux data and bitmask 175 to exclude data flagged with severe quality issues (Tenenbaum & Jenkins 2018).

For EBLM J2359+44 two RV measurements have been published by Poleski et al. (2010) that confirmed it to be a binary star. Full time series RV observations of EBLM J0719+25 and EBLM J2359+44 have been taken with the SOPHIE high-resolution echelle spectrograph (Perruchot et al. 2008), mounted on the 1.93-m telescope at the Observatoire de Haute-Provence in France as part of the Binaries Escorted By Orbiting Planets survey to search for circumbinary planets (Martin et al. 2019). For EBLM J0719+25, eight SOPHIE spectra have been obtained between 2018 November and 2019 October in high-resolution mode ($R = 75\,000$). For EBLM J2359+44, 15 SOPHIE spectra have been obtained between 2018 November and 2020 September in high-resolution mode ($R = 75\,000$) as well as in high-efficiency (HE) mode ($R = 40\,000$). The HE mode allows an about 2.5 times higher throughput compared to the high-resolution mode. The spectra have an average SNR of about 30 with a typical exposure time of 1800 s. To allow the removal of the background contamination from the Moon, all observations were taken with one fibre on target and one on the sky. The spectra were reduced using the SOPHIE data reduction software (Baranne et al. 1996) and RVs were measured by cross-correlation with a G2 mask (Courcol et al. 2015) for which we achieved a typical precision of 10 m s^{-1} for our spectra. All RV measurements are listed in the Appendix Tables B1 and B2. We submitted a target list of 40 EBLM systems from Triaud et al. (2017) as a priority 4 proposal to be observed with high-resolution spectrograph (Crause et al. 2014) of the *Southern African Large Telescope (SALT)* in medium resolution ($R \approx 37\,000$). In total, 30 of them were observed between the 2017 May 19 and August 7, including EBLM J0239−20. These observations were made in long-slit mode with an exposure time-scaling as a function of magnitude to ensure a SNR $\geq$ 100. Data were reduced and processed using standard pipelines (Craig et al. 2015; Crawford 2015) to produce two spectra for each observation (370–550 and 550–890 nm) as a result of the dual-beam nature of the spectrograph.

3. ANALYSIS

For data analysis, we followed the methods, described in SW21. Both *TESS* and *CHEOPS* light curves were modelled using the `qpower2` transit model, which applies a power-2 limb darkening law (Maxted & Gill 2019). We use it as binary star model including primary and secondary eclipses which is implemented in the python software `PYCHEOPS`[3] (Maxted et al. 2021). The parameters of the binary star model are the orbital period P, the mid-time of the primary eclipse T_0, the primary and secondary eclipse depths D and L, the impact parameter b, the parameters $f_c = \sqrt{e}\cos(\omega)$ and $f_s = \sqrt{e}\sin(\omega)$, which parametrize the eccentricity e and the longitude of periastron ω, the limb darkening parameters h_1 and h_2 (Maxted 2018), and W, which becomes the width of the eclipse for $e = 0$ and is defined by the stellar radii, impact parameter, and the semimajor axis a (see Maxted et al. 2021 for details). We used Gaussian priors for f_c, f_s. These priors were derived from RV measurements of the systems. Orbital parameters from RV measurements for EBLM J0239−20, EBLM J0540−17, and EBLM J0546−18 have been published in Triaud et al. (2017). Their eccentricities are reported to be consistent to zero, thus we set those priors to zero for all three systems. For EBLM J0719+25 and EBLM J2359+44, we used the binary star python code `ellc` (Maxted 2016), to model the RV from SOPHIE measurements as well as the two measurements from Poleski et al. (2010) for EBLM J2359+44. We sampled the posterior probability distribution (PPD) of our model parameters f_c, f_s, and the semi-amplitude K, using the Markov chain Monte Carlo (MCMC) code `EMCEE` (Foreman-Mackey et al. 2013) to take the RV-jitter of the data into account by weighting the fit by the log-likelihood function. For this we used the period from our *TESS* fit (see Section 3.1) as fixed prior and did not need to fit any additional trend to the data. The resulting orbital parameters, as well as the mass function $f(m)$ (see equation 6 in Triaud et al. 2017) are listed in Table 2. The resulting priors for f_c, f_s are listed in Table 3. The errors represent the one sigma error of the resulting PPD.

[3]https://github.com/pmaxted/pycheops

Table 2. Stellar and orbital parameters of the primary stars. Coordinates are in J2000.

	EBLM J0239−20	EBLM J0540−17	EBLM J0546−18	EBLM J0719+25	EBLM J2359+44
Name	TYC 5862-1683-1	TYC 5921-745-1	TIC 93334206	TYC1913-0843-1	TYC3245-0077-1
RA	02 39 29.29	05 40 43.58	05 46 04.81	07 19 14.26	23 59 29.74
Dec.	−20 02 24.0	−17 32 44.8	−18 17 54.6	+25 25 30.8	+44 40 31.2
G (mag)	10.57	11.42	12.01	11.15	10.46
Sp. type	G0	G0	G0	G0	F8
$T_{\rm eff,1}$(K)[a]	5758 ± 100	6290 ± 77	6180 ± 80	6026 ± 67	6799 ± 83
$\log g_1$(cgs)[c]	4.053 ± 0.016	4.058 ± 0.017	4.100 ± 0.034	4.239 ± 0.022	4.068 ± 0.010
[Fe/H][a]	0.27 ± 0.12	−0.04 ± 0.05	−0.45 ± 0.08	0.04 ± 0.05	0.12 ± 0.05
R_1($R_\odot$)[c]	1.587 ± 0.039	1.636 ± 0.040	1.509 ± 0.064	1.305 ± 0.038	1.711 ± 0.033
M_1($M_\odot$)[c]	1.037 ± 0.060	1.120 ± 0.062	1.051 ± 0.059	1.078 ± 0.059	1.253 ± 0.070
Orbital parameters:					
K(km s^{-1})	21.316 ± 0.036[d]	16.199 ± 0.010[d]	26.15 ± 0.10[d]	15.02 ± 0.04[b]	23.62 ± 0.08[b]
e	< 0.0032[d]	0.00029 ± 0.00057[d]	< 0.015[d]	0.0730 ± 0.0045[b]	0.4773 ± 0.0010[b]
ω(deg)	–	−164 ± 10[d]	–	−155.8 ± 5.4[b]	−94.290 ± 0.060[b]
$f(m)$ (10^{-3} $M_\odot$)	2.788 ± 0.014[d]	2.6444 ± 0.0096[d]	2.1332 ± 0.0023[d]	2.597 ± 0.021[b]	10.53 ± 0.11[b]

Notes.
[a]From spectral analysis.
[b]From RV analysis.
[c]From light-curve modelling.
[d]From Triaud et al. (2017).

Table 3. Priors on $f_c = \sqrt{e}\cos\omega$ and $f_s = \sqrt{e}\sin\omega$ used in the analysis of the *CHEOPS* and *TESS* light curves based on the spectroscopic orbits for each binary system.

Target	f_c	f_s
EBLM J0239−20	0.0	0.0
EBLM J0540−17	0.0	0.0
EBLM J0546−18	0.0	0.0
EBLM J0719+25	−0.247 ± 0.013	−0.111 ± 0.023
EBLM J2359+44	−0.0517 ± 0.0007	−0.6889 ± 0.0007

3.1 *TESS* light-curve analysis

Only segments of the *TESS* light curve within one eclipse duration of the time of mid-eclipse were used in this analysis. To remove trends in the light curve, we divided these segments by a linear polynomial model fitted to the data either side of the eclipse. Unlike SW21, we preferred this method over the use of a Gaussian process in order to securely preserve the transit shape of the faint secondary eclipses.

To model the light curve, we first determined the initial orbital parameters using a least-squares fit and then sampled the PPD of our transit model using `EMCEE`. We placed normal priors on the orbital parameters f_c, f_s, as listed in Table 3 as well as on the white noise, using the residual rms of the least-squares fit. The resulting parameters from the *TESS* light curves are detailed in Tables 4, 5, and 6. These represent the median of the PPD as well as the standard errors from the 15.9 and 84.1 per cent percentile-points of the PPD. We show the resulting fits of all targets in the Appendix, Figs D1, D2 and D3 .

3.2 *CHEOPS* light-curve analysis

CHEOPS light curves were analysed in two steps. First, we analysed every visit separately to derive initial model parameters (see Table 1 for an overview of all visits). As described in detail in SW21, instrumental effects like roll angle, contamination, and background level can be represented using linear correlation parameters or for roll angle ϕ, $\sin(\phi)$, $\cos(\phi)$, $\sin(2\phi)$, etc., which were iteratively selected.[4] The PPD of all model and decorellation parameters were sampled simultaneously using `EMCEE`. We used the same Gaussian priors for f_c, and f_s as for the *TESS* data and since we obtained single-eclipse events, we fixed our transit model to accurately measured orbital period P, from the *TESS* light-curve fit. For secondary eclipses, we used priors on the parameters D, W, and b, as derived from the primary eclipse of each target.

In a second step, we were using a single MCMC to perform a 'multivisit' analysis including all visits for a specific target. We used the same priors as for the individual analysis as well as the results as input parameters and used the function `multivisit` of `PYCHEOPS` to sample the joint PPD with `EMCEE`. Hereby we used the implicit decorrelation method for instrumental trends as described in Maxted et al. (2021), keeping the number of harmonic terms to its default ($N_{\rm roll} = 3$). The resulting parameters from the *CHEOPS* light curves are detailed in Tables 4, 5, and 6. These represent the median of the PPD as well as the standard errors from the 15.9 and 84.1 per cent percentile-points of the PPD. We show the resulting fits of all targets in the Appendix, Figs E1, E2, and E3 and in Table A1 the resulting decorrelation parameters from the multivisit analysis.

3.3 Stellar parameters

We used co-added high-resolution spectra to derive the stellar parameters of the primary components ($T_{\rm eff}$ and [Fe/H]). For EBLM J0540−17, we used co-added CORALIE spectra, obtained by Triaud et al. (2017) and available from the European Southern Observatory (ESO) science archive facility[5] and co-added SOPHIE spectra for EBLM J0719+25 and EBLM J2359+44. The stellar parameters for these three targets were derived using the equivalent width method following the same methodology, model atmospheres, and line list as described in Sousa (2014) and Santos et al. (2013). In here, we applied the `ARES` code (Sousa et al. 2015), as well as the `MOOG` radiative

[4]See Table A1 for the decorrelation parameters selected for each visit.
[5]http://archive.eso.org/

Table 4. The derived parameters for EBLM J0239-20 and EBLM J0540-17 using *CHEOPS* and *TESS* light-curve fits with eclipse depths being in the relevant instrumental bandpass.

	EBLM J0239−20		EBLM J0540−17	
	CHEOPS	*TESS*	*CHEOPS*	*TESS*
Model parameters				
T_0(BJD)	2163.70805 ± 0.00015	1413.46145 ± 0.00012	2209.12086 ± 0.00021	1470.51285 ± 0.00030
P (d)	2.778691 (fixed)	2.778691 ± 0.000001	6.004940 (fixed)	6.004940 ± 0.000003
D	0.01679 ± 0.00019	0.016716 ± 0.000092	0.01404 ± 0.00021	0.01381 ± 0.00018
W	0.05268 ± 0.00037	0.05286 ± 0.00015	0.03818 ± 0.00019	0.03827 ± 0.00018
b	0.654 ± 0.014	0.6428 ± 0.0092	0.167 ± 0.105	0.253 ± 0.089
f_c	0.0 (fixed)	0.0 (fixed)	0.0 (fixed)	0.0 (fixed)
f_s	0.0 (fixed)	0.0 (fixed)	0.0 (fixed)	0.0 (fixed)
L	$(3.68 \pm 0.45) \times 10^{-4}$	$(7.30 \pm 0.42) \times 10^{-4}$	$(3.66 \pm 0.53) \times 10^{-4}$	$(6.61 \pm 0.78) \times 10^{-4}$
h_1	0.766 ± 0.020	0.836 ± 0.011	0.767 ± 0.015	0.811 ± 0.013
h_2	0.47 ± 0.22	0.59 ± 0.20	0.54 ± 0.18	0.47 ± 0.21
Derived parameters				
R_2/R_1	0.12957 ± 0.00073	0.12929 ± 0.00035	0.11850 ± 0.00087	0.11752 ± 0.00075
R_1/a	0.1797 ± 0.0027	0.1788 ± 0.0015	0.1084 ± 0.0018	0.1105 ± 0.0023
R_2/a	0.02288 ± 0.00042	0.02289 ± 0.00024	0.01265 ± 0.00028	0.01264 ± 0.00034
i(°)	83.25 ± 0.24	83.40 ± 0.15	88.96 ± 0.67	88.40 ± 0.59
e	0.0	0.0	0.0	0.0
ω(°)	–	–	–	–
Absolute parameters				
a(AU)	0.04106 ± 0.00076	0.04107 ± 0.00076	0.0703 ± 0.0012	0.0703 ± 0.0012
R_2($R_\odot$)	0.2056 ± 0.0052	0.2041 ± 0.0044	0.1939 ± 0.0050	0.1959 ± 0.0056
M_2($M_\odot$)	0.1597 ± 0.0059	0.1597 ± 0.0059	0.1633 ± 0.0058	0.1634 ± 0.0058
log g_2(cgs)	5.015 ± 0.014	5.0214 ± 0.0076	5.075 ± 0.015	5.066 ± 0.019
$T_{\rm eff,2}$(K)	3027 ± 88	2982 ± 71	3220 ± 70	3143 ± 66

Table 5. The derived parameters for EBLM J0546−18 and EBLM J0719+25 using *CHEOPS* and *TESS* light-curve fits with eclipse depths being in the relevant instrumental bandpass.

	EBLM J0546−18		EBLM J0719+25	
	CHEOPS	*TESS*	*CHEOPS*	*TESS*
Model parameters				
T_0(BJD)	2203.71457 ± 0.00027	2174.98660 ± 0.00032	2216.39007 ± 0.00024	2559.38262 ± 0.00019
P (d)	3.191919 (fixed)	3.191919 ± 0.000034	7.456295 (fixed)	7.456295 ± 0.000045
D	0.0239 ± 0.0018	0.02328 ± 0.00081	0.02145 ± 0.00051	0.02092 ± 0.00017
W	0.0415 ± 0.0016	0.04020 ± 0.00047	0.02491 ± 0.00029	0.02456 ± 0.00018
b	0.777 ± 0.040	0.824 ± 0.013	0.498 ± 0.033	0.520 ± 0.016
f_c	0.0 (fixed)	0.0 (fixed)	-0.2589 ± 0.0069	-0.2588 ± 0.0053
f_s	0.0 (fixed)	0.0 (fixed)	-0.116 ± 0.023	-0.139 ± 0.022
L	$(11.0 \pm 1.3) \times 10^{-4}$	$(17.6 \pm 1.2) \times 10^{-4}$	$(6.4 \pm 1.2) \times 10^{-4}$	$(9.32 \pm 0.65) \times 10^{-4}$
h_1	0.44 ± 0.14[a]	0.719 ± 0.100	0.731 ± 0.020	0.813 ± 0.013
h_2	0.31 ± 0.14	0.37 ± 0.24	0.24 ± 0.24	0.56 ± 0.19
Derived parameters				
R_2/R_1	0.1546 ± 0.0059	0.1526 ± 0.0027	0.1465 ± 0.0018	0.144625 ± 0.000593
R_1/a	0.1533 ± 0.0057	0.1569 ± 0.0026	0.0757 ± 0.0017	0.076857 ± 0.001019
R_2/a	0.0223 ± 0.0014	0.02361 ± 0.00034	0.01076 ± 0.00033	0.010941 ± 0.000176
i(°)	83.17 ± 0.54	82.58 ± 0.22	87.84 ± 0.19	87.711 ± 0.100
e	0.0	0.0	0.0807 ± 0.0041	0.086242 ± 0.003542
ω(°)	–	–	-155.9 ± 4.6	-151.8 ± 4.3
Absolute parameters				
a(AU)	0.04587 ± 0.00080	0.04586 ± 0.00080	0.0802 ± 0.0014	0.0801 ± 0.0014
R_2($R_\odot$)	0.233 ± 0.013	0.2356 ± 0.0072	0.1912 ± 0.0060	0.1915 ± 0.0044
M_2($M_\odot$)	0.2129 ± 0.0075	0.2131 ± 0.0075	0.1584 ± 0.0056	0.1583 ± 0.0056
log g_2(cgs)	5.029 ± 0.047	5.020 ± 0.021	5.075 ± 0.023	5.073 ± 0.012
$T_{\rm eff,2}$(K)	3409 ± 111	3332 ± 90	3208 ± 89	3063 ± 40

Note.
[a]The limb darkening parameters are not well constrained from *CHEOPS* data for EBLM J0546−18 (see discussion in Section 4.2.1.).

Table 6. The derived parameters for EBLM J2359+44 using *CHEOPS* and *TESS* light-curve fits with eclipse depths being in the relevant instrumental bandpass.

	EBLM J2359+44	
	CHEOPS	*TESS*
Model parameters		
T_0(BJD)	1977.85239 ± 0.00015	1773.4230 ± 0.0027
P (d)	11.3627 (fixed)	11.3627 ± 0.0027
D	0.02997 ± 0.00016	0.03015 ± 0.00023
W	0.025946 ± 0.000091	0.02611 ± 0.00017
b	0.096 ± 0.024	0.141 ± 0.033
f_c	-0.05175 ± 0.00032	-0.05242 ± 0.00053
f_s	-0.68888 ± 0.00071	-0.68906 ± 0.00072
L	$(8.91 \pm 0.63) \times 10^{-4}$	$(20.21 \pm 0.98) \times 10^{-4}$
h_1	0.7754 ± 0.0043	0.8393 ± 0.0093
h_2	0.61 ± 0.13	0.60 ± 0.19
Derived parameters		
R_2/R_1	0.17311 ± 0.00045	0.17363 ± 0.00067
R_1/a	0.06971 ± 0.00033	0.07040 ± 0.00066
R_2/a	0.011990 ± 0.000077	0.01207 ± 0.00015
i(°)	89.619 ± 0.098	89.43 ± 0.14
e	0.47724 ± 0.00098	0.47755 ± 0.00099
ω(°)	-94.30 ± 0.027	-94.350 ± 0.044
Absolute parameters		
a(AU)	0.1144 ± 0.0020	0.1144 ± 0.0020
R_2($R_\odot$)	0.2963 ± 0.0058	0.3001 ± 0.0064
M_2($M_\odot$)	0.293 ± 0.010	0.293 ± 0.010
$\log g_2$(cgs)	4.9602 ± 0.0049	4.9490 ± 0.0089
$T_{\rm eff,2}$(K)	3465 ± 46	3513 ± 41

transfer code (Sneden et al. 2012), assuming ionization and excitation equilibrium of iron lines. For EBLM J0546−18, we used co-added CORALIE spectra and applied a wavelet decomposition method where we compare the coefficients from a wavelet decomposition to those from a grid of model spectra. Those model spectra were synthesized using the code SPECTRUM (Gray & Corbally 1994), MARCS model atmospheres (Gustafsson et al. 2008), as well as the atomic line list version 5 of the *Gaia* ESO survey (Heiter et al. 2015). The method is detailed in Gill, Maxted & Smalley (2018) and has been found to deliver robust measurements for effective temperature and metallicity for spectra with relatively low SNR (SNR $\gtrapprox$ 40). For EBLM J0239−20, we used the *SALT* spectra and modelled the stellar fundamental parameters using the software SME[6] (Spectroscopy Made Easy; Valenti & Piskunov 1996; Piskunov & Valenti 2017) that computes synthetic spectra with atomic and molecular line data from VALD[7] (Ryabchikova et al. 2015) which are compared to the observations. We chose the stellar atmosphere grid Atlas12 (Kurucz 2013) and modelled $T_{\rm eff}$, $\log g_1$, abundances and v sin i one parameter at a time. Due to the high rotational velocity ($v \sin i = 31 \pm 4\,{\rm km\,s^{-1}}$), the uncertainties in $\log g_1$ derived from the line wings of the Ca I triplet around 6200 Å is with 0.2 dex relatively high. We thus rely on the light-curve modelling to derive the surface gravity of our targets.

Similarly to SW21, we derived the system parameters using the function massradius in PYCHEOPS. As explained in Maxted et al. (2021), this function applies a Monte Carlo approach to derive basic system parameters like the primaries mean stellar density, the mass and radius of the M-dwarf, using the PPD of our *CHEOPS* light-curve fit. It additionally uses the primaries mass and radius, as well as the orbital parameters which were not sampled in the PPD-like period, and eccentricity as input and derives the surface gravity $\log g_2$ of the M-dwarf using the RV semi-amplitudes. We used this function to optimize the global system parameters in a two-stage iterative process.

In the first step, we used the primaries mass and radius estimates available from the *TESS* input catalogue v8 (Stassun et al. 2019) as initial parameters. The derivation of these estimates is based on an empirical relation including photometric effective temperature estimates for stars with well-measured *Gaia* distances. We used the same priors for period and eccentricity that we used for our *CHEOPS* fit, as well as the semi-amplitudes from RV measurements. For EBLM J0239−20, EBLM J0540−17, and EBLM J0546−18, we have used the published semi-amplitudes (Triaud et al. 2017). For EBLM J0719+25 and EBLM J2359+44, we use the results from our orbital fit (see Table 2).

In a second iteration, we made use of the massradius function again in order to find the best-fitting parameters of the primary mass and radius from our light-curve fit. We used the relation of Enoch et al. (2010) (equation 4), to derive a mass sample for the primary star. This sample is based on the stellar density samples obtained from the first iteration and created similar sized samples for $T_{\rm eff}$ and [Fe/H] based on our spectroscopic stellar parameters. We then added a normal distributed scatter of 0.023 to account for the resulting scatter for this relation found by Enoch et al. (2010). We derived a radius sample using this mass sample as well as the density sample. We used the mass and radius samples to re-run the massradius function to derive the final stellar parameters of the primary and M-dwarf components. We finally derived the surface gravity $\log g_1$ from the stellar density, directly measured from the light-curve fit of our *CHEOPS* data, as well as the primaries mass derived from the previous step.

We derived the effective temperature $T_{\rm eff,2}$ of the M-dwarf companion using the surface brightness ratio L/D, derived from the light-curve fit of primary and secondary eclipses. Similar to SW21, we derived the integrated surface brightness in the *CHEOPS* and *TESS* passbands of the primary star, using the spectral parameters $T_{\rm eff,2}$, $\log g_1$, and [Fe/H] using PHOENIX model atmospheres with no alpha-element enhancement (Husser et al. 2013) and sampled a large set of surface temperatures over the known parameters, L/D, $\log g$, and [Fe/H] (assuming similar metallicity for both companions) to derive the effective temperature.

The light contribution from the primary star reflected to the M-dwarf can be expressed by $A_{\rm g}(R_2/a)^2$, where $A_{\rm g}$ is the geometric albedo and R_2/a is the radius of the M-dwarfs in units of the semi-major axis, which we directly measure from our model. With a typical albedo of $A_{\rm g} \sim 0.1$ (Marley et al. 1999), the light contribution for our targets is very small and thus negligible. Nevertheless, for the two shortest period binaries in our sample, EBLM J0239−20 and EBLM J0546−18 the light contribution might cause an underestimation of the secondary eclipse depth on the one sigma level and thus an underestimation of $T_{\rm eff,2}$ in the order of 1 per cent for both *CHEOPS* and *TESS* passbands. Thus, we increased the relative uncertainties for $T_{\rm eff,2}$ for EBLM J0239−20 and EBLM J0546−18 by 1 per cent in order to account for the unknown uncertainty of $A_{\rm g}$.

All parameters of the primary stars are listed in Table 2, all parameters for the M-dwarf companions are listed in Tables 4, 5, and 6.

4. DISCUSSION

We have derived the stellar parameters for both companions for all of our targets thanks to high-precision *CHEOPS* light curves. For the M-dwarfs, we derive accurate radii with an average uncertainty of

[6] http://www.stsci.edu/~valenti/sme.html
[7] http://vald.astro.uu.se

3.2 ± 1.3 per cent and the surface gravity with an average uncertainty of 0.4 ± 0.3 per cent. This precision for the surface gravity of M-dwarfs is better then, or hardly reached with state-of-the-art high-resolution spectroscopic measurements of field M-dwarfs (e.g. Marfil et al. 2021; Olander, Heiter & Kochukhov 2021).

4.1 RV priors

We used priors obtained from the RV orbital parameters eccentricity (e) and longitude of periastron (ω) to fit our *CHEOPS* and *TESS* light curves. Only EBLM J0719+25 and EBLM J2359+44 have eccentricities significantly larger than zero, the others we have fixed to zero eccentricity. We analysed the effect of imposing RV priors on the *CHEOPS* parameter fit by repeating it with f_c and f_s kept as free parameters. Two of our binaries with previously fixed eccentricities, resulted in eccentricities consistent to zero with EBLM J0239−20 ($e = 0.028 \pm 0.058$) and EBLM J0546−18 ($e = 0.0005 \pm 0.0007$). For EBLM J0540−17 and EBLM J0719+25, this fit resulted in a longer MCMC chain, which finally ended with a less uniformly defined PPD for W, which was strongly correlated to f_c and f_s. This led to up to 5 per cent overestimated radii for the M-dwarfs. Except for these two stars, the derived model parameters did not deviate more than 1σ from the parameters listed in Tables 4, 5, and 6. Nevertheless, we found that for the orbital parameters all resulting uncertainties were about one order of magnitude larger then obtained from the RV fitting alone. We conclude that even for high-precision *CHEOPS* light curves, (i) RV measurements are essential to derive precise radii for low-mass eclipsing binaries and (ii) our analysis method does not allow constraining the orbital eccentricity from the light curves better than from RV measurements.

4.2 Comparison to *TESS*

For all targets, we compared our results from *TESS* light-curve fitting with the *CHEOPS* results. Both instruments comprise different passbands with the *TESS* having an redder effective wavelength of 745.6 nm compared to *CHEOPS* with 581.1 nm.[8] In this, we do not compare the limb darkening parameters and absolute eclipse depths, since these depend on the instrumental passband. The secondary eclipses are thus 1.5–2.5 times deeper in *TESS*, compared to *CHEOPS*. We find a good agreement on the derived radius ratio, inclination, and relative primary radii R_1/a (<1 per cent). As discussed in the previous section, using RV priors is essential to derive precise radii for the M-dwarfs. We find that keeping f_c and f_s as free parameters results in 3–6 per cent smaller radii for *TESS* light curves (for EBLM J0540−17 and EBLM J0719+25), compared to *CHEOPS*. Using similar RV priors (see Section 3.1), we find that the derived radii and surface gravity for the M-dwarfs agree well for all targets (on average within 0.9 and 0.15 per cent, respectively) between *TESS* and *CHEOPS*. We find that the uncertainties of the derived parameters from *TESS* light curves are of a similar order, compared to *CHEOPS* results. *TESS* is in favour, for relatively bright secondary companions with deep secondary eclipse and for targets with short orbital periods and thus, many eclipses covered during the monitoring. We find that the effective temperature of the M-dwarfs, derived from *TESS* light curves is in agreement with our *CHEOPS* value for EBLM J2359+44, but about 2–4 per cent cooler for our other targets. We included the result from SW21 for EBLM J1934−42 to analyse for any systematic difference between the effective temperature of the M-dwarf, derived with *TESS* relative to *CHEOPS*. We modelled a constant difference between two instruments using `EMCEE` to take the RV-jitter of the effective temperatures of both *TESS* and *CHEOPS* into account by weighting the fit by the log-likelihood function. The offset from our sample of six stars results in a slightly lower (1.11 ± 0.99 per cent) temperature for *TESS* light curves with a remaining jitter of 0.0076 per cent.

The small discrepancy in $T_{\rm eff,2}$ might be caused by an underestimation of the secondary eclipse depth (L). In Section 3.3, we have discussed that reflected light might lead to an underestimated depth of the secondary eclipse. Nevertheless, this effect affects both passbands of *CHEOPS* and *TESS* in a comparable level and only for the shortest period binaries in our sample. Thus, reflection cannot explain this discrepancy. Possible explanations might be uncertainties introduced by the stellar model we used to derive the temperature from the surface brightness, or stellar activity of the primary star, linked to stellar spots which are not accounted for in the eclipse model, we have used.

4.2.1 Limb darkening parameters

For our *CHEOPS* and *TESS* fits, we kept the limb darkening parameters h_1 and h_2 free. To compare our results, we derived expected limb darkening parameters for EBLM J0239−20, EBLM J0540−17, EBLM J0546−18, and EBLM J0719+25 by interpolating the tables for the *TESS* bandpass and Kepler passband (for *CHEOPS* data, respectively) published in Maxted (2018) using the stellar parameters $T_{\rm eff,1}$, $\log g_1$, and [Fe/H] as listed in Table 2, and applying an offset ($h_1 + 0.01$ and $h_2 - 0.045$; Maxted 2018). This method did not converge for the hottest star in our sample EBLM J2359+44 since its effective temperature exceeds the tabulated temperature range. Thus, we used the other four targets for this comparison. The expected limb darkening parameters are listed in Table C1. We find that h_1 agrees on average well with differences of a few per cent, while we find larger discrepancies for h_2 in the order of several 10 per cent similarly in the *CHEOPS* and *TESS* data sets. This finding, as well as the derived uncertainties follow the trend from Maxted (2018; fig 4), for h_2 to be about one order of magnitude less constrained than h_1. We find some cases of larger uncertainties in *CHEOPS* light-curve fits. In the case of EBLM J0546−18 we derived about 31 per cent uncertainty for h_1 and the derived parameter differs more than 70 per cent from the expectations. This is not surprising, given the large impact parameter which does not allow constraining the limb darkening parameters for this star. We have repeated the *CHEOPS* and *TESS* fits for these four targets, using the expected limb darkening parameters as priors, but found that introducing these priors will neither improve the fit, nor has it any significant impact on the derived M-dwarf parameters. We, thus, present in Table 5 the derived parameters without priors for h_1 and h_2, noting that the corresponding values are less well constrained with *CHEOPS* compared to *TESS*.

4.3 Mass–radius diagram

The main goal of the *CHEOPS* programme is to build a well-defined mass–radius diagram for stars below the fully convective boundary. In Fig. 1, we show our five targets together with the theoretical mass relation from MIST (MESA Isochrones & Stellar Tracks) stellar models for 1-Gyr stars of solar metallicity ([Fe/H] = 0.0) as well as for slightly more metal-rich stars ([Fe/H] = 0.25) (Paxton et al. 2011; Choi et al. 2016; Dotter 2016). Similarly to SW21, we

[8]Filter profiles and effective wavelengths can be accessed using the VSO Filter Profile Service.

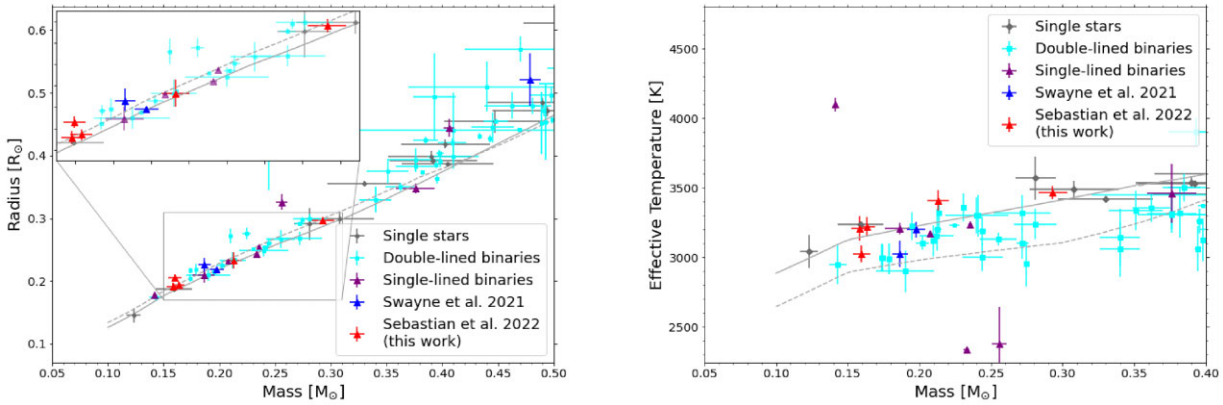

Figure 1. Left-hand panel: Mass–radius diagram for low-mass stars. Triangles: Single-lined eclipsing binaries, with *CHEOPS* programme targets highlighted in red and blue. Grey and cyan squares: Single stars and double-lined binaries from literature with measured mass, radius, and effective temperature. The zoom-in section highlights the MIST model tracks for [Fe/H] = 0, grey line, and [Fe/H] = 0.25, grey dotted line. Right-hand panel: Mass-effective temperature diagram of the same data set compared to same MIST models.

compiled a comparison sample of precisely measured low-mass stars from literature, classified in single stars, double-lined binaries, and single-lined binaries (Carter et al. 2011; Nefs et al. 2013; Gillen et al. 2017; Parsons et al. 2018; Smith et al. 2021; SW21). We compared the radii with both the MIST and the Exeter/Lyon (Baraffe et al. 2015) models for solar metallicity. The M-dwarf radius for EBLM J0239−20 is 11.0 ± 2.6 per cent (12.5 ± 2.6 per cent) larger for the MIST (and Exeter/Lyon) model, the others are on average 2.6 ± 1.3 per cent (3.5 ± 1.3 per cent) larger compared to both models. Despite most of our targets being within the uncertainties in agreement with the theoretical radii, we observe that they follow the trend of very low-mass stars to be slightly larger than predicted by models. In Fig. 1, we also show the effective temperature of our five M-dwarfs, the result from SW21, as well as the same literature sample. Our target's effective temperatures follow the overall trend of low-mass stars. We note that EBLM J0239−20, similarly to EBLM J1934−42 (blue triangle from SW21) have a slightly higher metallicity ([M/H] > 0.2). Both stars are slightly larger and cooler, compared to models for stars with solar metallicity. As shown in Fig. 1, this trend is predicted by the MIST models for more metal-rich stars. However, also in this case, both stars are slightly larger than predicted by models for higher metallicity stars. Fig. 1 shows three single-lined stars from literature with measured M-dwarf effective temperatures being outliers of more than 500 K compared to model predictions. These are KIC 1571511B (Ofir et al. 2012) as well as SAO 106989 and HD 24465 (Chaturvedi et al. 2018). Populating the low-mass main sequence with M-dwarfs having precise effective temperature measurements will help us to constrain possible trends for low-mass dwarfs. This is one of the main goals of our *CHEOPS* programme.

Magnetic activity of the primary star, like spot crossing is not accounted for in our eclipse model, thus, can affect the size determinations of the M-dwarfs. We used the *TESS* light curves to search for variability linked to magnetic activity, like rotational pattern and flares. No flares have been found in the *TESS* data set. EBLM J0239−20 shows a variable modulation of 2–3 per cent close to the orbital period, most probably linked to stellar activity aligned with the rotational period of the G-dwarf. All our other targets show no or small variability of less than 1 per cent. Since we found a good agreement between the M-dwarf radii in the different passbands of *TESS* and *CHEOPS*, we conclude that stellar activity can only have a minor (< 1 per cent) effect on the derived M-dwarf radius for the five stars, analysed in this work. Depending on the actual contrast between the primary star and the M-dwarf the contribution of the M-dwarf is between 300 and 1200 ppm in *CHEOPS* data. From this, we can exclude large flares with exceed relative intensities of 25–100 per cent compared to the M-dwarfs average brightness. M-dwarfs with such flaring activity exist but account only for about 10 per cent of the flaring M-dwarfs found in *TESS* (Günther et al. 2020). We can assume that the M-dwarf rotation period is synchronized with the orbital period, since the tidal synchronization time-scale for EBLM systems is about 1 Gyr or less (Barker 2020). Thus the M-dwarfs are expected to be fast rotators ($P \lesssim 10$ d), which are expected to show enhanced activity levels (e.g. Morales et al. 2010; Wright et al. 2018). Activity-induced photometric variations, observed for field M-dwarfs are typically in the order of 1 per cent of the M-dwarfs average brightness (Medina et al. 2020). This results in an expected photometric variability in the order of 10 ppm for active M-dwarfs which is below the detection efficiency in our data.

Reflected light from the primary star (see discussion in Section 3.3) can cause an underestimated radius of the M-dwarfs. We note that this effect is negligible for the five binaries analysed in this work, as it would result in a relative underestimation of about 100 ppm of the M-dwarfs radius for the shortest period binaries in our sample.

5. SUMMARY

Within the framework of our EBLM project, we initiated a *CHEOPS* observing programme of 23 low-mass stars to measure precise stellar parameters as well as effective temperatures. In this paper, we have analysed high-precision *CHEOPS* light curves of primary and secondary eclipses for five eclipsing binaries with low-mass companions. Using the `qpower2` transit model, of `PYCHEOPS`, we find an average uncertainty of 3.2 ± 1.3 per cent for the M-dwarfs radius and 0.4 ± 0.3 per cent for the M-dwarfs surface gravity. Thus, using precision light curves allowed us to overcome the larger uncertainties to derive stellar parameters typically involved with high-resolution spectroscopy. We have derived the M-dwarfs effective temperature from the contrast between primary and secondary eclipses and the metallicity from spectroscopic analysis of the primary star, assuming equal metallicities of both components.

This allows us to compare the M-dwarfs parameters to theoretical structural models, like the MIST models. We find that all our M-dwarfs are on average larger, but agree within the uncertainty with the model predictions. This is also true for low-mass M-dwarfs with enhanced metallicity, which follow the predicted trend of having a larger radius as well as a cooler effective temperature. Up to now, the stellar models, as well as our transit model do not include stellar activity. We have analysed *TESS* light curves for all our five targets and find a good (better than 1 per cent) agreement on the M-dwarf radius in the different passband of both instruments. Given the absence of strong activity indicated variability and flare activity as well as this good agreement, we conclude that stellar activity does not play a strong role in the derived uncertainties for our five stars. This result is of particular importance for more active stars on our *CHEOPS* programme, where activity-induced changes in parameters between the *TESS* and *CHEOPS* passbands might need to be accounted for. We have analysed the dependence of derived M-dwarf parameters with priors used in the fit. We find that limb darkening parameters as well as orbital parameters like the eccentricity and the argument of periastron are not well constrained from our model fit. Nevertheless, we find that, other than the limb darkening coefficients, precise orbital parameters, obtained from RV observations are crucial to derive M-dwarf radii better than 5 per cent.

Together with SW21, we increased the sample to eight low-mass stars, with precise measured radii from *CHEOPS* data. Due to the fact that the F,G,K-type primary companions are single-lined binaries, that allow high-precision orbital characterization as well as the determination of precise stellar parameters like metallicity, this survey, once completed, will allow us to empirically shed light on the radius inflation problem for very low-mass stars.

ACKNOWLEDGEMENTS

CHEOPS is an ESA mission in partnership with Switzerland with important contributions to the payload and the ground segment from Austria, Belgium, France, Germany, Hungary, Italy, Portugal, Spain, Sweden, and the UK. The *CHEOPS* Consortium would like to gratefully acknowledge the support received by all the agencies, offices, universities, and industries involved. Their flexibility and willingness to explore new approaches were essential to the success of this mission. Spectroscopic data were obtained via observing time allocations at OHP awarded by the French PNP (18B.PNP.SAN1 and 19A.PNP.SANT). Some of the observations reported in this paper were obtained with the *Southern African Large Telescope (SALT)*. This research has made use of the services of the ESO Science Archive Facility. This research is also supported from the European Research Council's (ERC) the European Union's Horizon 2020 research and innovation programme (grant agreement no 803193/BEBOP). PM acknowledges support from STFC research grant number ST/M001040/1. MIS acknowledges support from STFC grant number ST/T506175/1. SGS acknowledges support from FCT through FCT contract no. CEECIND/00826/2018 and POPH/FSE (EC). SH gratefully acknowledges CNES funding through the grant 837319. YA and MJH acknowledge the support of the Swiss National Fund under grant 200020_172746. We acknowledge support from the Spanish Ministry of Science and Innovation and the European Regional Development Fund through grants ESP2016-80435-C2-1-R, ESP2016-80435-C2-2-R, PGC2018-098153-B-C33, PGC2018-098153-B-C31, ESP2017-87676-C5-1-R, and MDM-2017-0737, Unidad de Excelencia Maria de Maeztu-Centro de Astrobiología (INTA-CSIC), as well as the support of the Generalitat de Catalunya/CERCA programme. The MOC activities have been supported by the ESA contract No. 4000124370. SCCB acknowledges support from FCT through FCT contracts no. IF/01312/2014/CP1215/CT0004. XB, SC, DG, MF, and JL acknowledge their role as ESA-appointed *CHEOPS* science team members. AB was supported by the SNSA. ACC acknowledges support from STFC consolidated grant numbers ST/R000824/1 and ST/V000861/1, and UKSA grant number ST/R003203/1. This project was supported by the CNES. The Belgian participation to *CHEOPS* has been supported by the Belgian Federal Science Policy Office (BELSPO) in the framework of the PRODEX Program, and by the University of Liège through an ARC grant for Concerted Research Actions financed by the Wallonia-Brussels International. LD is an F.R.S.-FNRS Postdoctoral Researcher. This work was supported by FCT - Fundação para a Ciência e a Tecnologia through national funds and by FEDER through COMPETE2020 - Programa Operacional Competitividade e Internacionalizacão by these grants: UID/FIS/04434/2019, UIDB/04434/2020, UIDP/04434/2020, PTDC/FIS-AST/32113/2017, POCI-01-0145-FEDER- 032113, PTDC/FIS-AST/28953/2017, POCI-01-0145-FEDER-028953, PTDC/FIS-AST/28987/2017, and POCI-01-0145-FEDER-028987. ODSD is supported in the form of work contract (DL 57/2016/CP1364/CT0004) funded by national funds through FCT. B-OD acknowledges support from the Swiss National Science Foundation (PP00P2-190080). This project has received funding from the European Research Council (ERC) under the European Union's Horizon 2020 research and innovation programme (project FOUR ACES; grant agreement No. 724427). It has also been carried out in the frame of the National Centre for Competence in Research PlanetS supported by the Swiss National Science Foundation (SNSF). DE acknowledges financial support from the Swiss National Science Foundation for project 200021_200726. MF and CMP gratefully acknowledge the support of the Swedish National Space Agency (DNR 65/19, 174/18). DG gratefully acknowledges financial support from the CRT Foundation under Grant No. 2018.2323 'Gaseous or rocky? Unveiling the nature of small worlds'. MG is an F.R.S.-FNRS Senior Research Associate. KGI is the ESA *CHEOPS* Project Scientist and is responsible for the ESA *CHEOPS* Guest Observers Programme. She does not participate in, or contribute to, the definition of the Guaranteed Time Programme of the *CHEOPS* mission through which observations described in this paper have been taken, nor to any aspect of target selection for the programme. This work was granted access to the HPC resources of MesoPSL financed by the Region Ile de France and the project Equip@Meso (reference ANR-10-EQPX-29-01) of the programme Investissements d'Avenir supervised by the Agence Nationale pour la Recherche. ML acknowledges support of the Swiss National Science Foundation under grant number PCEFP2_194576. For Italy, *CHEOPS* activities have been supported by the Italian Space Agency, under the programs:ASI-INAF n. 2013-016-R.0 and ASI-INAF n. 2019-29-HH.0. This work was also partially supported by a grant from the Simons Foundation (PI Queloz, grant number 327127). IRI acknowledges support from the Spanish Ministry of Science and Innovation and the European Regional Development Fund through grant PGC2018-098153-B-C33, as well as the support of the Generalitat de Catalunya/CERCA programme. GyMSz acknowledges the support of the Hungarian National Research, Development and Innovation Office (NKFIH) grant K-125015, a PRODEX Institute Agreement between the ELTE Eötvös Loránd University and the European Space Agency (ESA-D/SCI-LE-2021-0025), the Lendület LP2018-7/2021 grant of the Hungarian Academy of Science and the support of the city of Szombathely. VVG is an F.R.S-FNRS Research Associate. NAW

acknowledges UKSA grant ST/R004838/1. VK acknowledges support from NSF award AST2009501. This work was also supported by the STFC PATT Travel grant ST/S001301/1. We thank the reviewer for valuable comments and suggestions.

This research is based on observations collected at the Observatoire de Haute-Provence (CNRS, France) and at the Southern African Large Telescope *(SALT)*.

DATA AVAILABILITY

All *CHEOPS* data and data products are publicly available via the Data Analysis Center for Exoplanets web platform. This paper includes data collected by the *TESS* mission, which is publicly available from the Mikulski Archive for Space Telescopes (MAST) at the Space Telescope Science Institute (STScI; https://mast.stsci.edu). Funding for the *TESS* mission is provided by the NASA Explorer Program directorate. STScI is operated by the Association of Universities for Research in Astronomy, Inc., under NASA contract NAS 5-26555. We acknowledge the use of public *TESS* Alert data from pipelines at the *TESS* Science Office and at the *TESS* Science Processing Operations Center. SOPHIE high-resolution spectra are available through the data archives of the Observatoire de Haute-Provence via http://atlas.obs-hp.fr/. Programme ID were 18B.PNP.SAN1 and 19A.PNP.SANT.

REFERENCES

Baraffe I., Homeier D., Allard F., Chabrier G., 2015, A&A, 577, A42
Baranne A. et al., 1996, A&AS, 119, 373
Barclay T., Pepper J., Quintana E. V., 2018, ApJS, 239, 2
Barker A. J., 2020, MNRAS, 498, 2270
Benz W. et al., 2021, Exp. Astron., 51, 109
Berger D. H. et al., 2006, ApJ, 644, 475
Carter J. A. et al., 2011, Science, 331, 562
Casagrande L., Flynn C., Bessell M., 2008, MNRAS, 389, 585
Chabrier G., Baraffe I., 1997, A&A, 327, 1039
Chabrier G., Gallardo J., Baraffe I., 2007, A&A, 472, L17
Chaturvedi P., Sharma R., Chakraborty A., Anandarao B. G., Prasad N. J. S. S. V., 2018, AJ, 156, 27
Choi J., Dotter A., Conroy C., Cantiello M., Paxton B., Johnson B. D., 2016, ApJ, 823, 102
Courcol B. et al., 2015, A&A, 581, A38
Craig M. W. et al., 2015, Astrophysics Source Code Library, record ascl:1510.007
Crause L. A. et al., 2014, in Ramsay S. K., McLean I. S., Takami H., eds, Proc. SPIE Conf. Ser. Vol. 9147, Ground-based and Airborne Instrumentation for Astronomy V. SPIE, Bellingham, p. 91476T
Crawford S. M., 2015, Astrophysics Source Code Library, record ascl:1511.005
Delrez L. et al., 2018, in Marshall H. K., Spyromilio J., eds, Proc. SPIE Conf. Ser. Vol. 10700, Ground-based and Airborne Telescopes VII. SPIE, Bellingham, p.
Donati J. F. et al., 2020, MNRAS, 498, 5684
Dotter A., 2016, ApJS, 222, 8
Dotter A., Chaboyer B., Jevremović D., Kostov V., Baron E., Ferguson J. W., 2008, ApJS, 178, 89
Dressing C. D., Charbonneau D., 2013, ApJ, 767, 95
Enoch B., Collier Cameron A., Parley N. R., Hebb L., 2010, A&A, 516, A33
Foreman-Mackey D., Hogg D. W., Lang D., Goodman J., 2013, PASP, 125, 306
Gill S., Maxted P. F. L., Smalley B., 2018, A&A, 612, A111
Gill S. et al., 2019, A&A, 626, A119
Gillen E., Hillenbrand L. A., David T. J., Aigrain S., Rebull L., Stauffer J., Cody A. M., Queloz D., 2017, ApJ, 849, 11
Gillon M. et al., 2016, Nature, 533, 221
Gray R. O., Corbally C. J., 1994, AJ, 107, 742
Günther M. N. et al., 2019, Nature Astron., 3, 1099
Günther M. N. et al., 2020, AJ, 159, 60
Gustafsson B., Edvardsson B., Eriksson K., Jørgensen U. G., Nordlund, Å., Plez B., 2008, A&A, 486, 951
Heiter U. et al., 2015, Phys. Scr., 90, 054010
Hoyer S., Guterman P., Demangeon O., Sousa S. G., Deleuil M., Meunier J. C., Benz W., 2020, A&A, 635, A24
Husser T. O., Wende-von Berg S., Dreizler S., Homeier D., Reiners A., Barman T., Hauschildt P. H., 2013, A&A, 553, A6
Jenkins J. M. et al., 2016, in Chiozzi G., Guzman J. C., eds, Proc. SPIE Conf. Ser. Vol. 9913, Software and Cyberinfrastructure for Astronomy IV. SPIE, Bellingham, p. 99133E
Kaltenegger L., Traub W. A., 2009, ApJ, 698, 519
Kesseli A. Y., Muirhead P. S., Mann A. W., Mace G., 2018, AJ, 155, 225
Kurucz R. L., 2013, Astrophysics Source Code Library, record ascl:1303.024
Marfil E. et al., 2021, A&A, 656, A162
Marley M. S., Gelino C., Stephens D., Lunine J. I., Freedman R., 1999, ApJ, 513, 879
Martin D. V. et al., 2019, A&A, 624, A68
Maxted P. F. L., 2016, A&A, 591, A111
Maxted P. F. L., 2018, A&A, 616, A39
Maxted P. F. L., Gill S., 2019, A&A, 622, A33
Maxted P. F. L. et al., 2021, MNRAS, in press, preprint (arXiv:2111.08828)
Medina A. A., Winters J. G., Irwin J. M., Charbonneau D., 2020, ApJ, 905, 107
Morales J. C. et al., 2009, ApJ, 691, 1400
Morales J. C., Gallardo J., Ribas I., Jordi C., Baraffe I., Chabrier G., 2010, ApJ, 718, 502
Morley C. V., Kreidberg L., Rustamkulov Z., Robinson T., Fortney J. J., 2017, ApJ, 850, 121
Mullan D. J., MacDonald J., 2001, ApJ, 559, 353
Nefs S. V. et al., 2013, MNRAS, 431, 3240
Nutzman P., Charbonneau D., 2008, PASP, 120, 317
Ofir A., Gandolfi D., Buchhave L., Lacy C. H. S., Hatzes A. P., Fridlund M., 2012, MNRAS, 423, L1
Olander T., Heiter U., Kochukhov O., 2021, A&A, 649, A103
Parsons S. G. et al., 2018, MNRAS, 481, 1083
Paxton B., Bildsten L., Dotter A., Herwig F., Lesaffre P., Timmes F., 2011, ApJS, 192, 3
Perruchot S. et al., 2008, in McLean I. S., Casali M. M., eds, Proc. SPIE Conf. Ser. Vol. 7014, Ground-based and Airborne Instrumentation for Astronomy II. SPIE, Bellingham, p. 70140J
Piskunov N., Valenti J. A., 2017, A&A, 597, A16
Poleski R., McCullough P. R., Valenti J. A., Burke C. J., Machalek P., Janes K., 2010, ApJS, 189, 134
Pollacco D. L. et al., 2006, PASP, 118, 1407
Quirrenbach A. et al., 2019, Mem. Soc. Astron. Ital., 90, 554
Ribas I., 2006, Ap&SS, 304, 89
Ricker G. R. et al., 2015, J. Astron. Telesc. Instrum. Syst., 1, 014003
Ryabchikova T., Piskunov N., Kurucz R. L., Stempels H. C., Heiter U., Pakhomov Y., Barklem P. S., 2015, Phys. Scr., 90, 054005
Santos N. C. et al., 2013, A&A, 556, A150
Smith G. D. et al., 2021, MNRAS, 507, 5991
Sneden C., Bean J., Ivans I., Lucatello S., Sobeck J., 2012, Astrophysics Source Code Library, record ascl:1202.009
Sousa S. G., 2014, Determination of Atmospheric Parameters of B. Springer International Publishing, Cham, p. 297
Sousa S. G., Santos N. C., Adibekyan V., Delgado-Mena E., Israelian G., 2015, A&A, 577, A67
Spada F., Demarque P., Kim Y. C., Sills A., 2013, ApJ, 776, 87
Stassun K. G. et al., 2019, AJ, 158, 138
Swayne M. I. et al., 2021, MNRAS, 506, 306 (SW21)
Tenenbaum P., Jenkins J. M., 2018, Technical Report 20180007935, Tess Science Data Products Description Document: Exp-Tess-Arc-Icd-0014 Rev D. NASA, Ames Research Center, CA
Torres G., Andersen J., Giménez A., 2010, A&AR, 18, 67
Triaud A. H. M. J. et al., 2013, A&A, 549, A18

Triaud A. H. M. J. et al., 2017, A&A, 608, A129
Valenti J. A., Piskunov N., 1996, A&AS, 118, 595
von Boetticher A. et al., 2019, A&A, 625, A150
Wright N. J., Newton E. R., Williams P. K. G., Drake J. J., Yadav R. K., 2018, MNRAS, 479, 2351
Zechmeister M. et al., 2019, A&A, 627, A49

APPENDIX A: DECORRELATION PARAMETERS FITTED FROM CHEOPS FITS

Table A1. Decorrelation parameters fitted from *CHEOPS* multivisit analysis for each visit (in the same order as in Table 1). The parameters are: image background level (dfdbg), PSF centroid position (dfdx and dfdy), time (dfdt), and aperture contamination (dfdcontam).

Target	Eclipse	dfdbg (10^{-3})	dfdx (10^{-4})	dfdy (10^{-3})	dfdt (10^{-2}d^{-1})	dfdcontam (10^{-3})
EBLM J0239−20	Primary	–	–	–	–	–
	Secondary	1.57 ± 0.90	–	0.311 ± 0.085	2.924 ± 0.029	–
	Secondary	1.21 ± 0.23	–	–	1.680 ± 0.029	–
EBLM J0540−17	Primary	1.20 ± 0.82	7.33 ± 1.79	–	-0.31 ± 0.43	–
	Secondary	0.71 ± 0.77	–	–	–	–
	Secondary	–	–	-0.51 ± 0.14	0.163 ± 0.036	–
	Secondary	–	5.95 ± 1.71	-0.87 ± 0.17	–	–
EBLM J0546−18	Primary	4.80 ± 0.87	–	0.78 ± 0.23	–	-1.73 ± 0.56
	Secondary	–	–	–	–	-1.59 +/− 0.83
	Secondary	2.85 ± 0.66	11.32 ± 2.51	–	1.367 ± 0.079	–
EBLM J0719+25	Primary	–	–	–	-0.496 ± 0.060	–
	Secondary	1.22 ± 0.93	–	–	0.291 ± 0.061	–
	Secondary	–	–	–	–	–
EBLM J2359+44	Secondary	0.83 ± 0.40	–	0.208 ± 0.088	–	-0.48 ± 0.27
	Primary	0.83 ± 0.26	–	–	–	–

APPENDIX B: RV MEASUREMENTS

Table B1. RV measurements for EBLM J0719+25.

BJD - 2400000	RV (km s^{-1})	RV error (km s^{-1})	Source
58436.57258	− 5.9492	0.0079	SOPHIE
58438.59676	12.5703	0.0057	SOPHIE
58536.40291	11.1258	0.0058	SOPHIE
58538.42658	− 9.091	0.012	SOPHIE
58542.39085	10.1391	0.0047	SOPHIE
58562.39379	− 15.9404	0.0073	SOPHIE
58566.37826	10.2797	0.0053	SOPHIE
58761.63689	− 3.306	0.011	SOPHIE

Table B2. RV measurements for EBLM J2359+44.

BJD - 2400000	RV (km s^{-1})	RV error (km s^{-1})	Source
53310.6391	− 19.07	0.42	Poleski et al.
53311.7990	− 26.36	0.50	Poleski et al.
58436.31776	− 33.537	0.011	SOPHIE
58438.40839	2.8147	0.0086	SOPHIE
58685.56693	− 29.4759	0.012	SOPHIE
58704.54724	− 8.063	0.014	SOPHIE
58729.61888	− 20.846	0.013	SOPHIE
58734.5406	11.81	0.015	SOPHIE
58754.47118	− 33.987	0.015	SOPHIE
58765.46162	− 31.893	0.011	SOPHIE
59030.57795	10.110	0.011	SOPHIE
59043.50347	1.726	0.014	SOPHIE
59045.53151	− 9.040	0.012	SOPHIE
59071.56389	− 27.920	0.012	SOPHIE
59077.5554	1.898	0.012	SOPHIE
59094.51791	− 29.440	0.011	SOPHIE
59100.57485	0.226	0.012	SOPHIE

APPENDIX C: EXPECTED LIMB DARKENING COEFFICIENTS

Table C1. Expected limb darkening coefficients derived for *TESS* and *CHEOPS* passbands.

Target	*CHEOPS*		*TESS*	
	h_1	h_2	h_1	h_2
EBLM J0239−20	0.743 ± 0.012	0.40 ± 0.05	0.798 ± 0.012	0.39 ± 0.05
EBLM J0540−17	0.773 ± 0.011	0.41 ± 0.05	0.826 ± 0.011	0.38 ± 0.05
EBLM J0546−18	0.771 ± 0.011	0.41 ± 0.05	0.822 ± 0.011	0.37 ± 0.05
EBLM J0719+25	0.754 ± 0.011	0.41 ± 0.05	0.808 ± 0.011	0.39 ± 0.05

APPENDIX D: *TESS* FITS

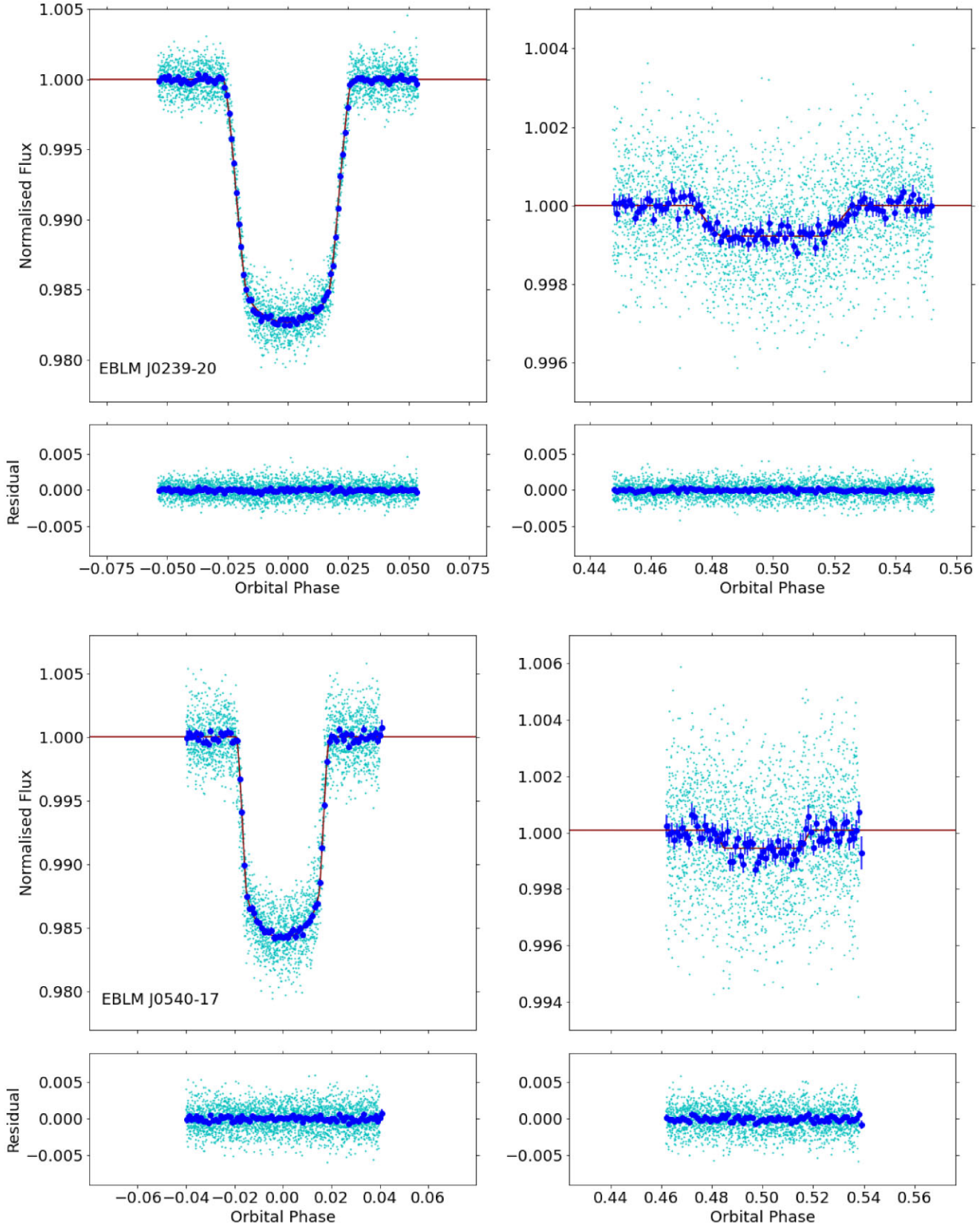

Figure D1. Fitted *TESS* light curves of all targets in phase intervals around the primary and secondary eclipse events. The observed data points are shown in cyan. The fitted light curve is shown in red. The residual of the fit is displayed below the fitted curves.

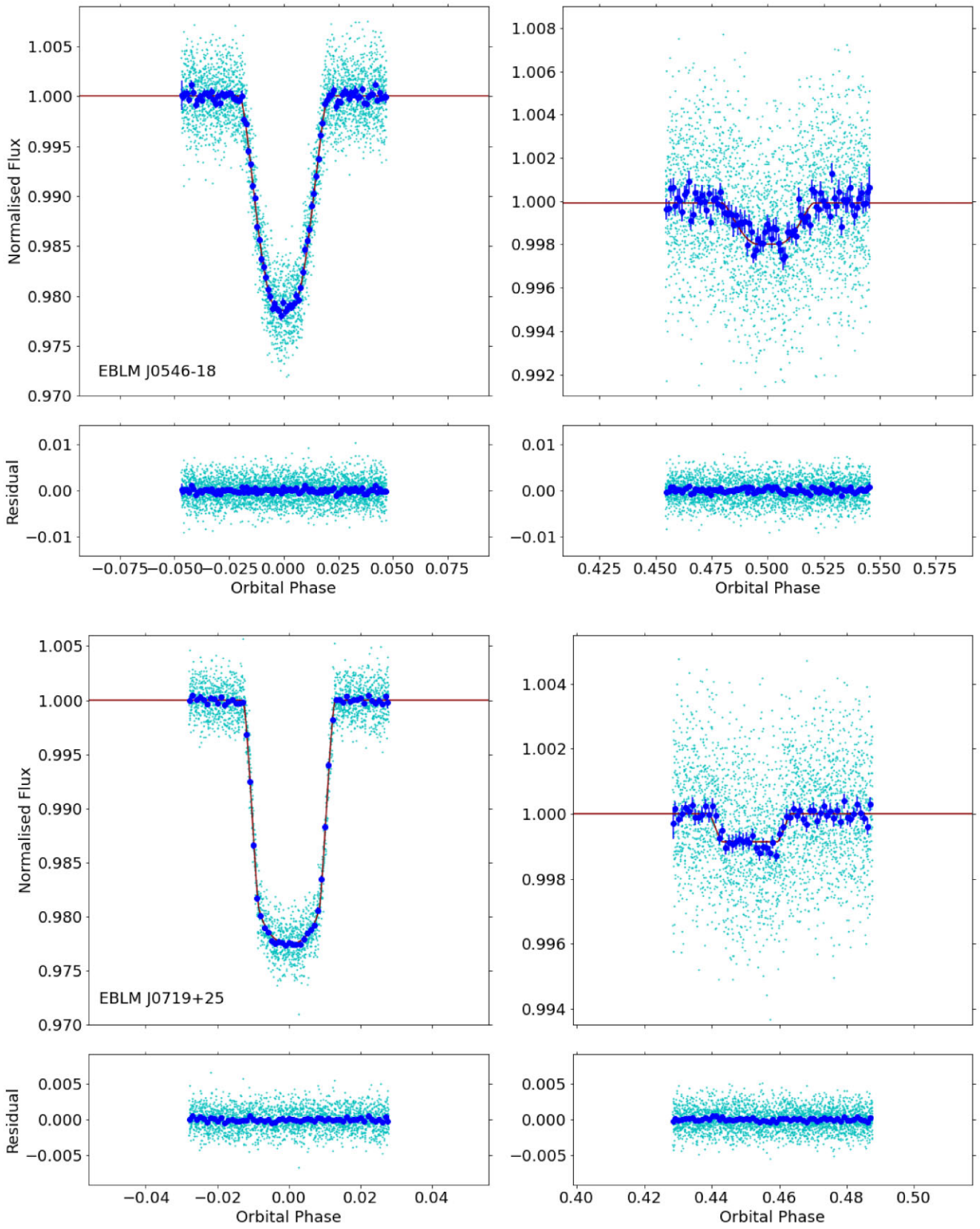

Figure D2. Fitted *TESS* light curves of all targets in phase intervals around the primary and secondary eclipse events. The observed data points are shown in cyan. The fitted light curve is shown in red. The residual of the fit is displayed below the fitted curves.

APPENDIX E: *CHEOPS* FITS

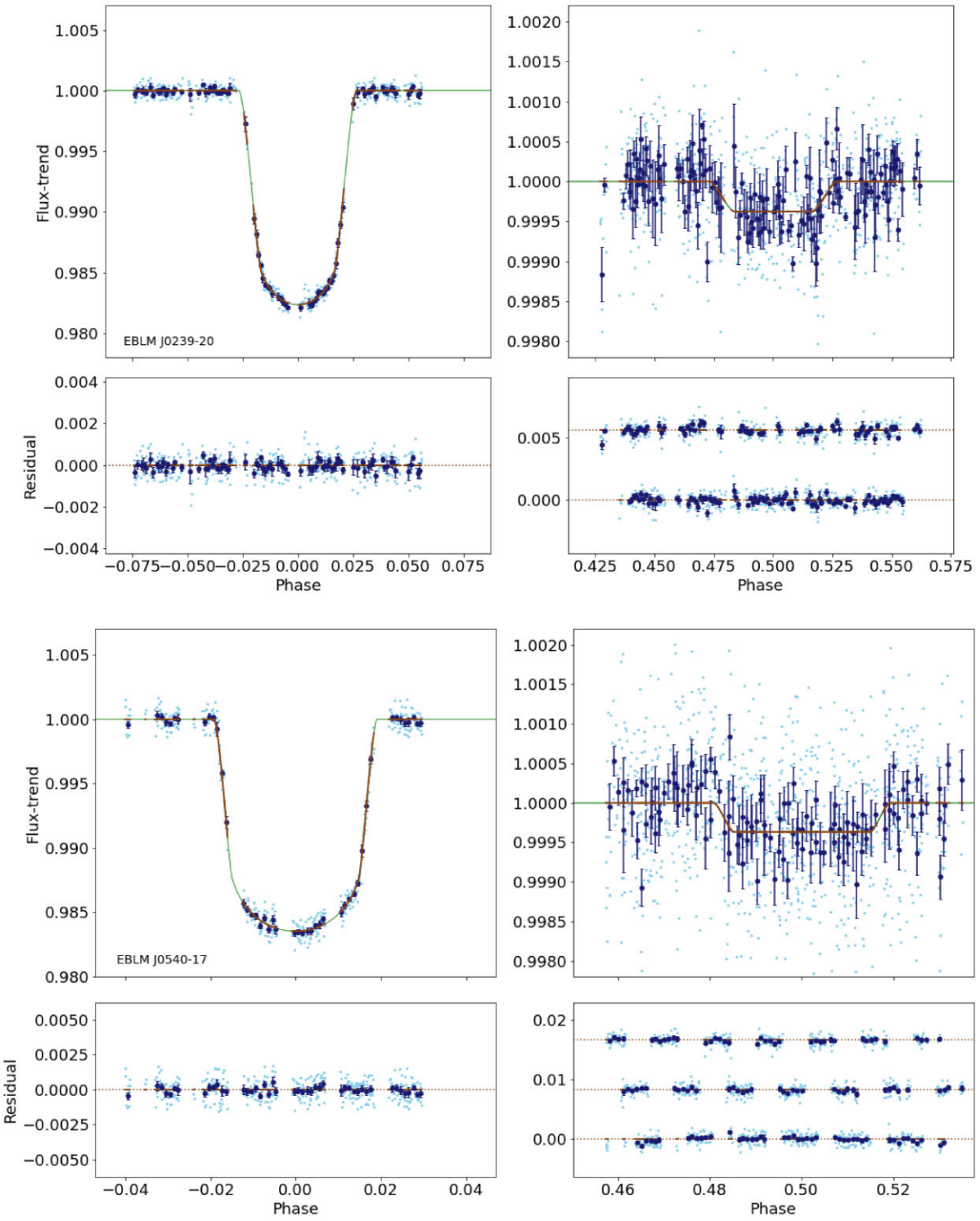

Figure E1. Fitted *CHEOPS* light curves of all targets in phase intervals around the primary and secondary eclipse events. The observed data points are shown in cyan. The fitted light curve is shown in red. The residual of the fit is displayed in blue below the fitted curves.

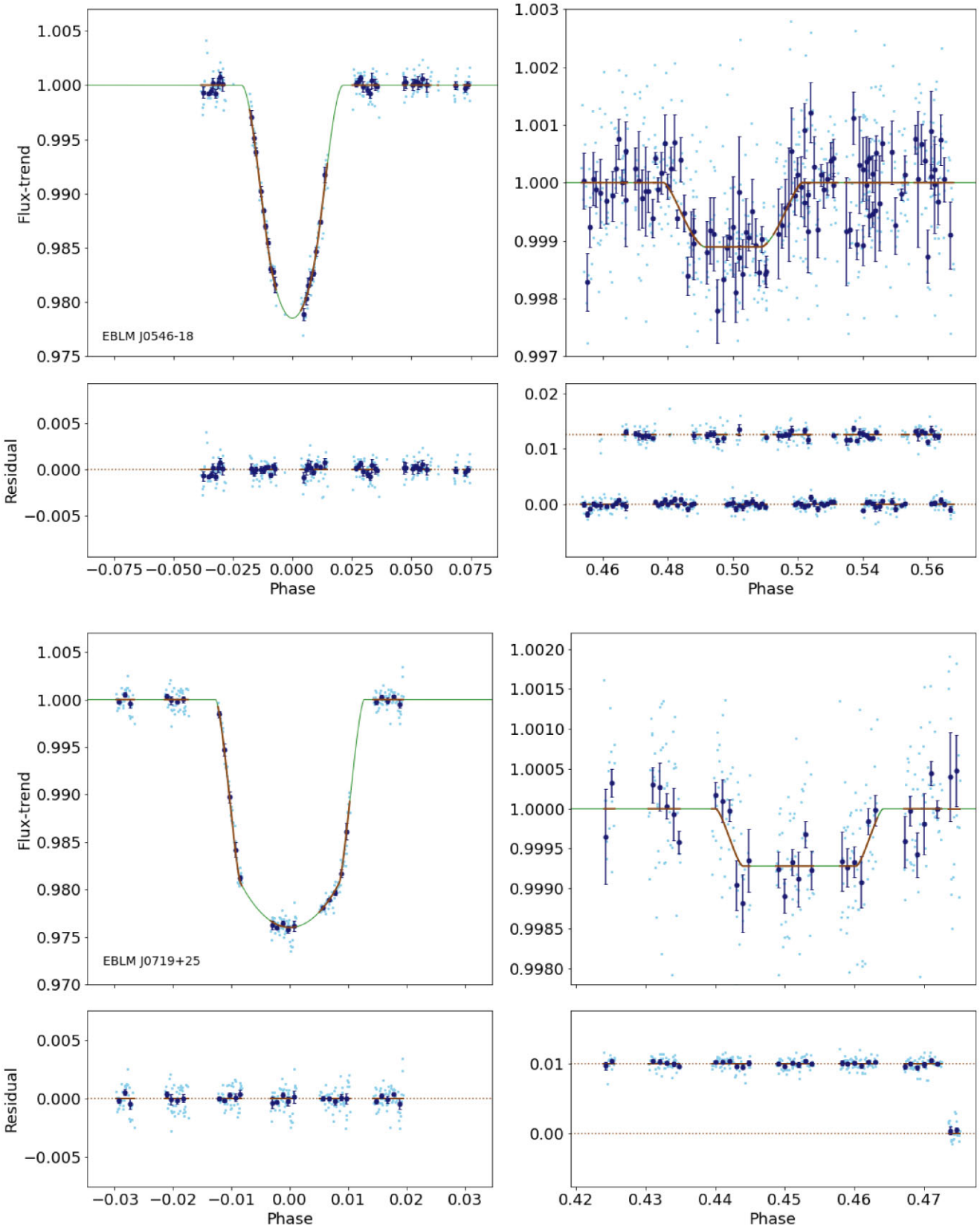

Figure E2. Fitted *CHEOPS* light curves of all targets in phase intervals around the primary and secondary eclipse events. The observed data points are shown in cyan. The fitted light curve is shown in red. The residual of the fit is displayed in blue below the fitted curves.

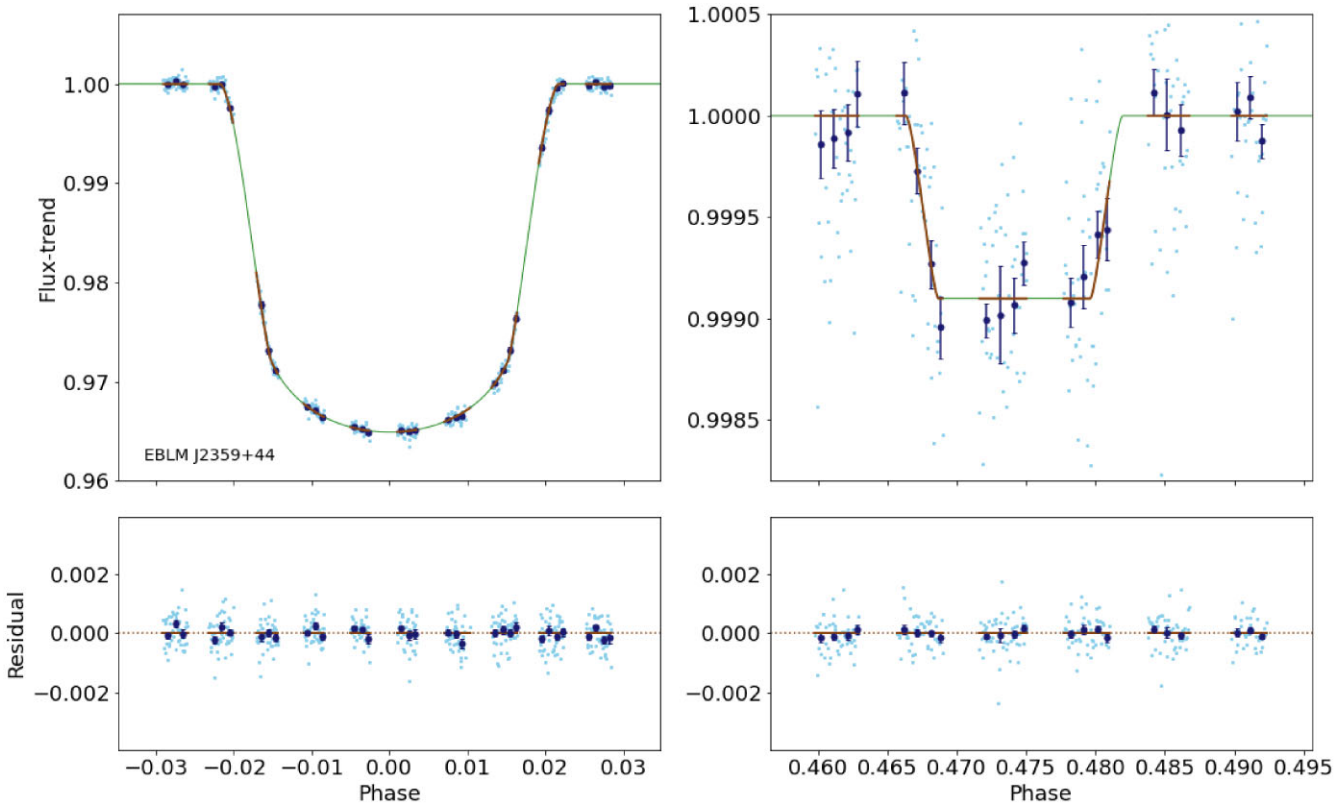

Figure E3. Fitted *CHEOPS* light curves of all targets in phase intervals around the primary and secondary eclipse events. The observed data points are shown in cyan. The fitted light curve is shown in red. The residual of the fit is displayed in blue below the fitted curves.

[1]*School of Physics & Astronomy, University of Birmingham, Edgbaston, Birmimgham B15 2TT, UK*
[2]*Astrophysics Group, Keele University, Staffordshire ST5 5BG, UK*
[3]*Instituto de Astrofisica e Ciencias do Espaco, Universidade do Porto, CAUP, Rua das Estrelas, P-4150-762 Porto, Portugal*
[4]*Department of Astronomy, Stockholm University, AlbaNova University Center, SE-10691 Stockholm, Sweden*
[5]*Observatoire Astronomique de l'Université de Genève, Chemin Pegasi 51, CH-1290 Versoix, Switzerland*
[6]*Aix Marseille University, CNRS, CNES, LAM, 38 rue Frédéric Joliot-Curie, F-13388 Marseille, France*
[7]*Department of Physics, University of Warwick, Gibbet Hill Road, Coventry CV4 7AL, UK*
[8]*Department of Astronomy, The Ohio State University, 4055 McPherson Laboratory, Columbus, OH 43210, USA*
[9]*Department of Space, Earth and Environment, Chalmers University of Technology, Onsala Space Observatory, SE-43992 Onsala, Sweden*
[10]*Physikalisches Institut, University of Bern, Gesellsschaftstrasse 6, CH-3012 Bern, Switzerland*
[11]*Instituto de Astrofisica de Canarias, E-38200 La Laguna, Tenerife, Spain*
[12]*Departamento de Astrofisica, Universidad de La Laguna, E-38206 La Laguna, Tenerife, Spain*
[13]*Institut de Ciencies de l'Espai (ICE, CSIC), Campus UAB, Can Magrans s/n, E-08193 Bellaterra, Spain*
[14]*Institut d'Estudis Espacials de Catalunya (IEEC), E-08034 Barcelona, Spain*
[15]*ESTEC, European Space Agency, NL-2201AZ Noordwijk, the Netherlands*
[16]*Admatis, 5. Kandó Kálmán Street, 3534 Miskolc, Hungary*
[17]*Departamento de Astrofisica, Centro de Astrobiologia (CSIC-INTA), ESAC Campus, E-28692 Villanueva de la Cañada (Madrid), Spain*
[18]*Departamento de Fisica e Astronomia, Faculdade de Ciencias, Universidade do Porto, Rua do Campo Alegre, P-4169-007 Porto, Portugal*
[19]*Space Research Institute, Austrian Academy of Sciences, Schmiedlstrasse 6, A-8042 Graz, Austria*
[20]*Center for Space and Habitability, Gesellsschaftstrasse 6, CH-3012 Bern, Switzerland*
[21]*INAF, Osservatorio Astronomico di Padova, Vicolo dell'Osservatorio 5, I-35122 Padova, Italy*
[22]*Université Grenoble Alpes, CNRS, IPAG, F-38000 Grenoble, France*
[23]*Institute of Planetary Research, German Aerospace Center (DLR), Rutherfordstrasse 2, D-12489 Berlin, Germany*
[24]*Université de Paris, Institut de physique du globe de Paris, CNRS, F-75005 Paris, France*
[25]*Centre for Exoplanet Science, SUPA School of Physics and Astronomy, University of St Andrews, North Haugh, St Andrews KY16 9SS, UK*
[26]*Centre for Mathematical Sciences, Lund University, Box 118, SE-221 00 Lund, Sweden*
[27]*Astrobiology Research Unit, Université de Liège, Allée du 6 Août 19C, B-4000 Liège, Belgium*
[28]*Space sciences, Technologies and Astrophysics Research (STAR) Institute, Université de Liège, Allée du 6 Août 19C, B-4000 Liège, Belgium*
[29]*Leiden Observatory, University of Leiden, PO Box 9513, NL-2300 RA Leiden, the Netherlands*
[30]*Dipartimento di Fisica, Universita degli Studi di Torino, via Pietro Giuria 1, I-10125 Torino, Italy*
[31]*University of Vienna, Department of Astrophysics, Türkenschanzstrasse 17, A-1180 Vienna, Austria*
[32]*Institut d'astrophysique de Paris, UMR7095 CNRS, Université Pierre & Marie Curie, 98bis blvd. Arago, F-75014 Paris, France*

[33]*Science and Operations Department - Science Division (SCI-SC), Directorate of Science, European Space Agency (ESA), European Space Research and Technology Centre (ESTEC), Keplerlaan 1, NL-2201-AZ Noordwijk, the Netherlands*
[34]*Konkoly Observatory, Research Centre for Astronomy and Earth Sciences, 1121 Budapest, Konkoly Thege Miklós út 15-17, Hungary*
[35]*ELTE Eötvös Loránd University, Institute of Physics, Pázmány Péter sétány 1/A, 1117, Hungary*
[36]*IMCCE, UMR8028 CNRS, Observatoire de Paris, PSL Univ., Sorbonne Univ., 77 av. Denfert-Rochereau, F-75014 Paris, France*
[37]*INAF, Osservatorio Astrofisico di Catania, Via S. Sofia 78, I-95123 Catania, Italy*
[38]*Institute of Optical Sensor Systems, German Aerospace Center (DLR), Rutherfordstrasse 2, D-12489 Berlin, Germany*
[39]*Dipartimento di Fisica e Astronomia 'Galileo Galilei', Universita degli Studi di Padova, Vicolo dell'Osservatorio 3, I-35122 Padova, Italy*
[40]*ETH Zurich, Department of Physics, Wolfgang-Pauli-Strasse 2, CH-8093 Zurich, Switzerland*
[41]*Cavendish Laboratory, JJ Thomson Avenue, Cambridge CB3 0HE, UK*
[42]*Center for Astronomy and Astrophysics, Technical University Berlin, Hardenberstrasse 36, D-10623 Berlin, Germany*
[43]*Institut für Geologische Wissenschaften, Freie Universität Berlin, D-12249 Berlin, Germany*
[44]*ELTE Eötvös Loránd University, Gothard Astrophysical Observatory, 9700 Szombathely, Szent Imre h. u. 112, Hungary*
[45]*MTA-ELTE Exoplanet Research Group, 9700 Szombathely, Szent Imre h. u. 112, Hungary*
[46]*Institute of Astronomy, University of Cambridge, Madingley Road, Cambridge CB3 0HA, UK*
[47]*Lowell Observatory, 1400 W. Mars Hill Rd., Flagstaff, AZ 86001, USA*

This paper has been typeset from a TEX/LATEX file prepared by the author.